JGR Oceans

In memory of our dear colleague and friend Prof. Mathieu Rouault who pioneered the idea for the study presented in this paper.

Key Points:
- Two latitudinal bands of minimum eddy energy spectra were found in the study region and appear to limit the eddies growth in size
- A critical latitude emerged around 11°S and suggests a transition of mesoscale regimes from nonlinear eddies to linear waves
- Eddy nonlinearity and lifespan increased poleward with decreasing size and the anticyclones trapped more chlorophyll than the cyclones

Correspondence to:
I. Halo,
ihalo@dffe.gov.za

Mesoscale Variability, Critical Latitude and Eddy Mean Properties in the Tropical South-East Atlantic Ocean

Issufo Halo[1,2] ⓘ, **Roshin P. Raj**[3] ⓘ, **Anton Korosov**[3] ⓘ, **Pierrick Penven**[4] ⓘ, **Johnny A. Johannessen**[5] ⓘ, and **Mathieu Rouault**[2]

[1]Department of Forestry, Fisheries and the Environment, Oceans and Coasts Research, Cape Town, South Africa, [2]Department of Oceanography, Nansen-Tutu Centre for Marine Environmental Research, University of Cape Town, Cape Town, South Africa, [3]Nansen Environmental and Remote Sensing Centre, Bjerknes Center for Climate Research, Bergen, Norway, [4]University Brest, CNRS, IRD, Ifremer, Laboratoire d'Océanographie Physique et Spatiale (LOPS), IUEM, Brest, France, [5]Nansen Environmental and Remote Sensing Centre, Geophysical Institute, University of Bergen, Bergen, Norway

Abstract Equatorward decrease of mesoscale eddy abundance, and meridional variations of their mean properties in the tropical South-East Atlantic Ocean have been investigated on the basis of horizontal length-scales of geostrophic flows, and theories of two-dimensional geostrophic turbulence on a β-plane. Meridional variations of satellite-derived altimetric eddy kinetic energy density spectra were assessed in bins of 5°, from 5°S to 25°S, zonally averaged between 8°W and 15°E. They revealed two latitudinal bands of minimum eddy energy spectra: one in the northern Angola Basin (5°S–10°S) and the other across the Angola Benguela Front (15°S–20°S). In the latter, both the eddy forcing scale and the Rhines scale were observed at wavelengths of 300 and 350 km respectively, suggesting that only a small spectral range exists for eddies to grow. On the other hand, in the former, the eddy forcing scale and the Rhines scale were observed at wavelengths of 454 and 520 km respectively. The ratio between the Rhines scale and the first baroclinic Rossby radius revealed an onset of a critical latitude at about 11.4°S. Consistently, maps of eddy frequency of occurrence computed from eddies identified in the region has shown a notable decay in signal of the eddy density distribution around that latitude. This could explain the sharp equatorward transition of mesoscale processes observed in this region, which seems to shift from nonlinear eddies to linear Rossby waves, potentially explaining why fewer eddies are observed in the region when compared to other regions of the world oceans.

Plain Language Summary In this study we analyzed oceanic flow variability across the range of oceanic intermediate length-scale ($\sim$10–400 km). We show that at about 11.4°S oceanic processes at intermediate scale shifts equatorward from a vortex-dominated to wave-dominated regimes. Such transition seems to provide answers to why relatively fewer vortex-structures are usually found in the tropical South East Atlantic Ocean when compared against similar regions of the world oceans. The census conducted on the vortex population in the region revealed that their prevalence increased poleward, statistically consistent with the increase of the vortices ability to conserve their structures more effectively.

1. Introduction

The large-scale upper ocean circulation in the tropical South-East Atlantic is characterized by the presence of a complex system of currents and countercurrents in both zonal and meridional directions (Peterson & Stramma, 1991; Schouten et al., 2005). Streamlines of long-term mean dynamic topography (Rio et al., 2011), commonly used as proxy of large-scale geostrophic circulation (Stammer et al., 2002) captures well many of these flow structures (Figure 1), and allows to relate their geographical positions with the smaller-scale mesoscale features.

This general circulation encompasses branches of the westward flowing South Equatorial Current (SEC) that stretches across a wider latitudinal band in the east, nearly between 2°N and 20°S. The SEC itself can be regarded as a system in its own, including a southern (SSEC), a central (CSEC), an equatorial (ESEC) and a northern (NSEC) components (Stramma & England, 1999). In addition, the overall circulation system also includes an eastward flowing Equatorial Undercurrent (EUC), and the South Equatorial Undercurrent (SEUC), both nearly confined over a latitudinal band between the equator and 5°S, as nicely illustrated in the diagram produced by Stramma and England (1999). Furthermore the circulation involves two opposite directed meridional coastal
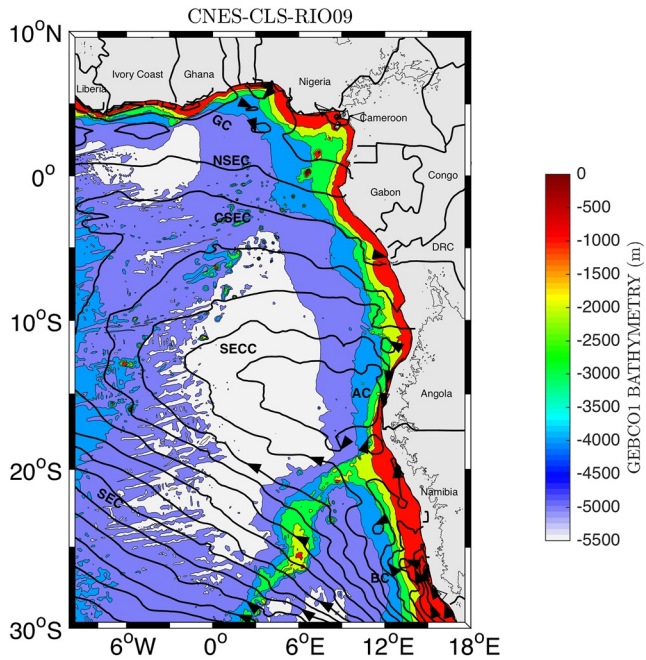
Figure 1. Streamlines of mean dynamic topography (MDT) derived from the French National Centre for Spatial Studies (CNES), and Collecte Localisation Satellites (CLS), release version of the year 2009 (CNES-CLS09), depicting ocean surface geostrophic circulation in the Tropical South East Atlantic region. The spacing between the contours is 2.5 cm, and the arrows indicate the direction of the currents. Inserted figure labels follow Stramma and England (1999): Guinea Current (GC), Northern South Equatorial Current (NSEC), Central South Equatorial Current (CSEC), South Equatorial Countercurrent (SECC), Southern South Equatorial Current (SSEC), Angola Current (AC) and Benguela Current (BC). The background shading colors represent the seafloor topography, derived from the Global Earth Bathymetric Chart of the Oceans (GEBCO 1).

flows (Figure 1) with remarkably distinct hydrographic characteristics: the poleward flowing warmer Angola Current (AC), that receives its warm waters from the eastward Equatorial Guinea Current (GC) and the equatorward colder Benguela Current (BC) that receives its waters from the South Atlantic Current (SAC), which flows eastward along the subtropical front, around 40°S. To the east of 0°longitude, a prominent cyclonic Angola gyre dominates the Angola Basin, between 5°N and 15°S. Both BC and AC converge and forms a sharp nearly zonal oceanic front termed the Angola-Benguela Frontal Zone (ABFZ), around 15°–20°S, which plays an important role on local biology, fishery and local rainfall distribution (Rouault et al., 2003).

On the mesoscale range, a train of westward propagation of sea surface height (SSH) anomalies have been frequently observed in this region and attributed to linear baroclinic Rossby waves (Grodsky & Carton, 2006; Illig et al., 2004; Kongue et al., 2017; Rouault et al., 2007; Schouten et al., 2005). However, on the basis of a regional ocean model, while investigating the internal variabilities of the ABFZ, Colberg and Reason (2007) suggested that this westward propagation of SSH anomalies are more eddy-like structures rather than waves. Nevertheless the occurrence of eddies in the ABFZ had been previously alleged by Stander (1964), and thereafter by Fillipov and Kolesnikov (1971). An attempt to quantify them was carried-out by Meeuwis and Lutjeharms (1990), using weekly maps of satellite derived sea surface temperatures (SST) ranging from year 1983–1985. More recently, eddy abundance and seasonality, as well as their hydrographic properties have been investigated by H. M. A. Aguedjou et al. (2019) and H. Aguedjou et al. (2021), respectively on the basis of the recent multimission satellite altimetry observations and Argo profiling floats, over a relatively larger geographical domain (70°W–10°E, 30°S–30°N). The identification of several mesoscale eddies in this region (H. M. A. Aguedjou et al., 2019), which under the same flow regime has been known as Rossby waves dominated, suggests that the flow field in the region is more complex than previously thought. Thus the need for robust criteria to discriminate eddies from waves, as well as complementary analysis of eddy properties in the region are required.

Distinguishing between Rossby waves and eddies from satellite maps of SSH has always been a difficult task because of the sampling requirements in time and space (Chelton et al., 2007; Chelton & Schlax, 1996; Quartly et al., 2006; Willett et al., 2006). It has been reported that in spatially low-resolution maps of SSH (e.g., fields from single pass satellite), eddies can be masquerade as Rossby waves, because eddies can drift westwards with similar predicted propagation phase-speed of linear Rossby waves (McWilliams & Flierl, 1979).

Merging of few simultaneously operating satellite altimeters allows to successfully investigate the eddy field and distinguish them from the linear Rossby waves, either on the basis of nonlinearity property of coherent geophysical flow structures (Chelton et al., 2007; Chelton, Schlax, & Samelson, 2011; Early et al., 2011; Klocker & Abernathey, 2014), or on the basis of sequential spectral signal filtering techniques as documented by Paulo and Sato (2015).

Different from linear waves, nonlinear eddies can trap material in their cores for many months and transport it for long distances, on scales of kilometers (Chelton, Schlax, & Samelson, 2011; Robinson, 1983). Thus water parcels with typical characteristics such as physical, chemical and biological, can be isolated from their background oceanic environment, drive biogeochemical processes, and form unique ecosystem regime (Mahadevan, 2014). Furthermore, through vertical suction of deep nutrient-rich waters into the upper photic oceanic layer, eddies can enhance photosynthetic processes, thus increasing oceanic primary productivity (Gruber et al., 2011; Lathuilière et al., 2011; McGillicuddy et al., 2007). Nevertheless eddies can also reduce coastal ocean biological productivity through a lateral off-shore transport of nutrients from the coast to the open ocean (Gruber et al., 2011), or through a downward pumping of surface nutrients to deep aphotic oceanic layers.

For the reasons highlighted above, and others, notably, eddies are geophysical structures capable to influence significantly the ecological composition of the marine ecosystems across several trophic levels, and water mass structures. Therefore it is important that eddies are properly assessed and characterized at regional scales, if the nature and extension of their influence/impact is to be properly understood.

Unfortunately, studies on eddies in the tropical South-East Atlantic Ocean are scanty. It has been traditionally reserved for the subtropical realms, south of 30°S, that is, in the Cape Basin (Doglioli et al., 2007; Duncombe-Rae et al., 1996; Hall & Lutjeharms, 2011; Nencioli et al., 2018), because of their contribution to the Agulhas leakage, which is thought to have a global-scale impact on the earth's climate system (Beal et al., 2011; Biastoch, Böning, & Lutjeharms, 2008; Biastoch, Lutjeharms, et al., 2008). Therefore in this study we aim to assess the mesoscale eddy variability in this region, in order to complement the previous studies and enhance the current understanding of the regional oceanography.

Fortunately, in recent years unprecedented upgrade of altimetry products derived from advanced algorithms and merging techniques, combining arrays of many existing altimetry tracks, spanning for more than two-decades (see Section 2), has led to improvements and better representation of the mesoscale eddy field and its variability across the global ocean. For example, an addition of 37% of more eddies have been retrieved in eastern boundary upwelling systems (Capet et al., 2014).

Using this upgraded satellite altimetry product, in this study we investigate: (a) the length-scales of the flow variability, (b) the eddy occurrence and their properties, and (c) the critical latitude at which eddy growth is halted in the tropical South-East Atlantic Ocean. The study has the following structure: In Section 2, we describe the different datasets and methods, including the eddy detection algorithm and the collocation methods applied to the altimetric identified eddies, Argo-float and satellite derived chlorophyll concentrations. The main results and findings are presented and discussed in Section 3 and the conclusions are summarized in Section 4.

2. Data Sets and Methods

2.1. Satellite Altimetry

The maps of Absolute Dynamic Topography (MADT) and derived geostrophic velocities (Rio et al., 2011) used in this study are part of the reprocessed altimetry product which have been released since 2014 (https://www.aviso.altimetry.fr/en/index.php?id=3622). The period covered here is 24 years, starting from 1 January 1993 to 31 December 2017. The product is delivered in delayed time (DT, i.e., at best 2-months after the measurement time), and contains level-4 SSH above the geoid, computed from all available altimeter missions, over the global ocean (AVISO, 2015).

The data set is gridded at a geospatial resolution of 25 × 25 km in a Cartesian grid, and provided at daily temporal resolution. The reprocessing techniques used allows to accurately extend the spatial coverage of the data set up to 10–15 km close to the coast (Pujol et al., 2016). This allows to assess mesoscale eddies relatively closer to the shelf environment. To deal with sub-grid scale processes, a 10% noise floor of the signal variance was used to take into account the small scale variability which can not be mapped and should be filtered in the analysis. The mapping procedure uses optimal interpolation schemes with realistic correlation functions at a given date. The data set is produced by the French institutions: National Centre for Spatial Studies (CNES), Collecte Localisation Satellites (CLS), and freely distributed online via the Copernicus Marine Services (https://data.marine.copernicus.eu/product/SEALEVEL_GLO_PHY_L4_MY_008_047/). The product is known to improve significantly the estimation of mesoscale signals when compared to the previous versions of the product (Capet et al., 2014; Pujol et al., 2016). As such, we expect to observe an improved eddy field in our region of interest.

2.1.1. Eddies From Altimetry Maps

Mesoscale ocean eddies are ubiquitous features in the oceans. To assess the statistics and characteristics of the eddy field in our region of interest, we used the automatic hybrid eddy detection algorithm presented by Halo et al. (2014). Because of its robust features, the algorithm has been used successfully in many studies in several oceanic basins, as in the equatorial north Atlantic Gulf of Guinea (Djakouré et al., 2014), and more recently in the Lofoten Basin (Raj et al., 2015, 2016). As described by Halo et al. (2014), the algorithm uses simultaneously geometric and dynamical properties of the flow field to identify an eddy. The geometric component regards a closed circular contour of the streamlines of the SSH (η). Whereas the dynamical property regards the

instantaneous flow field within the closed contour of the SSH, where the vorticity field dominates the strain rate or deformed flow field, following the Okubo-Weiss formulation: $W = S_n^2 + S_s^2 - \zeta^2$. Where vorticity is defined as $\zeta = \frac{\partial v}{\partial x} - \frac{\partial u}{\partial y}$, and the strain includes both normal S_n and shear S_s components expressed as $S_n = \frac{\partial u}{\partial x} - \frac{\partial v}{\partial y}$, and $S_s = \frac{\partial v}{\partial x} + \frac{\partial u}{\partial y}$. The u and v represent horizontal components of geostrophic velocities in x and y directions, estimated from variations of η, using the relations: $u = -\frac{g}{f}\frac{\partial \eta}{\partial y}$ and $v = \frac{g}{f}\frac{\partial \eta}{\partial x}$. Here g and f represent the acceleration due to gravity (9.81 m s^{-2}) and the Coriolis parameter ($f = 2\,\Omega.\sin\phi$). The eddies are tracked in time and space with reference to the position of their centers, following the method proposed by Penven et al. (2005), whereby an eddy retains its identity between consecutive time-frames if a generalized distance between the eddies center in a non-dimensional property space is minimum. For details, see Halo et al. (2014).

2.2. Satellite Ocean-Color

The satellite-based ocean color product used in this study has been derived from the Ocean Color Climate Change Initiative (OC CCI, https://esa-oceancolour-cci.org/) project (Brewin, 2015; Lavender et al., 2015). The project aims at providing the best ocean color essential climate variables (ECVs) data, based on a merging scheme of data retrieved from spaceborne optical sensors including: The MEdium Resolution Imaging Spectrometer (MERIS) on Envisat, operated by the European Space Agency (ESA), and both the MODerate resolution Imaging Spectroradiometer (MODIS), and the Sea-viewing Wide Field of View Sensor (SeaWIFS), operated by the National Aeronautics and Space Administration (NASA). The product is robust as it benefits from an improved bias correction, cloud masks algorithms, and more reliable automated quality assurance process.

2.2.1. Chlorophyll-a Within the Eddies

Daily values of surface chlorophyll concentration were extracted from the daily OC CCI, using the Nansat, a Python toolbox for geospatial data (Korosov et al., 2016). To colocate the concentrations of chlorophyll within the altimetric eddies, the coordinates of ocean eddies were converted to pixel/line coordinates on the OC CCI products using Nansat (Korosov et al., 2016). The chlorophyll values were computed as averages of all valid pixels from the day corresponding to the altimeter-based eddy observation, located around the eddy from the center to the rim.

2.3. Argo-Floats

To derive the hydrographic vertical structure through the water column of the mesoscale eddies identified in the altimetry maps, we have utilized the in-situ measurements retrieved by the Argo profiling floats http://www.argo-datamgt.org/Access-to-data/Argo-data-selection. Argo is an international program, a global array of free-drifting floats that profiles the upper 2,000 m of the oceanic water column, measuring temperature, salinity and pressure, every 10 day. For quality control purposes the data is validated against high-resolution hydrographic casts from ship-surveys, using the conductivity temperature depth (CTD) profilers. The quality controlled data are freely available by the international Argo program, and its associated national programs in many countries. The data used here is in delayed mode, extracted from a global domain and has a temporal coverage spanning from 1997 to 2017.

2.3.1. Argo-Floats Within the Eddies

The method implemented by Raj et al. (2016) was used to identify Argo-floats observed within the altimetry eddy's domain. At first order the positions of the Argo floats are tested against the longitude and latitude center positions of the corresponding daily altimetry eddies, both cyclones and anticyclones. To successfully distinguish eddy polarities (i.e., cyclonic and anticyclonic eddies) through their vertical structures captured by the Argo-floats only floats located at a distance that is within half eddy radius are selected. A total number of 74 Argo floats have been identified within the eddies: 42 cyclonic and 32 anticyclonic.

2.4. WOA18

The baroclinic Rossby radius of deformation used in this study was computed using the statistical and objectively analyzed in situ oceanic mean temperature (Locarnini et al., 2019), and salinity (Zweng et al., 2019) profiles, through the water column, derived from the World Ocean Atlas data set, released in the year 2018 (WOA18).
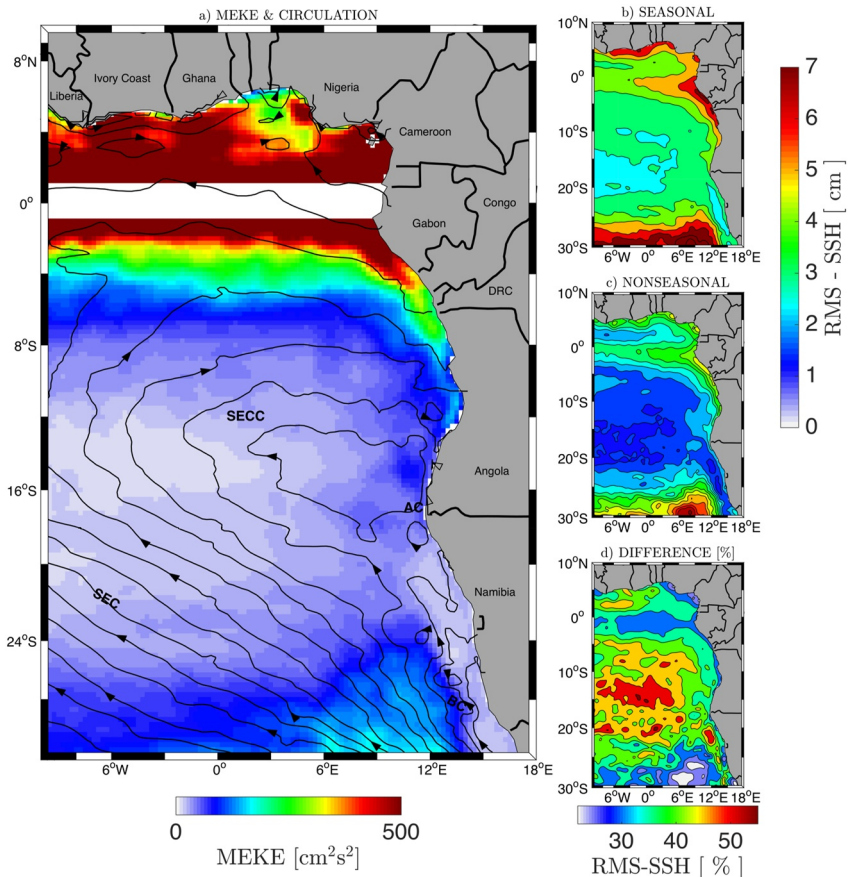
Figure 2. Oceanic mesoscale eddy and variability in the tropical East Atlantic Ocean. (a) Mean eddy kinetic energy, it portrays the bulk measure of mesoscale activity. (b) Seasonal mesoscale variability expressed by root mean square of sea surface height. (c) Same as in (b) but with seasonality removed. The seasonality was removed by extracting the seasonal anomalies as in Marchesiello et al. (2003) and Penven et al. (2005), in our case with reference to the four austral seasons. (d) Difference between seasonal and non-seasonal influences expressed in percentage. All maps have been computed from daily satellite altimetry measurements spanning from 1993 to 2017.

WOA18 is quality controlled data set, covering a time period that spans from 1955 to 2017. The product includes annual, seasonal, and monthly climatologies. Temperature and salinity are gridded globally in a mesh size of $1/4° \times 1/4°$, in longitude and latitude dimensions; while the other parameters are gridded in a mesh size of $1° \times 1°$. The product has been regarded as being better than all its previous versions. It is freely available from the World Ocean Database center https://www.ncei.noaa.gov/archive/accession/NCEI-WOA18.

3. Results and Discussion

Figure 2a shows the bulk measure of mesoscale activity, expressed by the mean eddy kinetic energy:

$$MEKE = \frac{\overline{u'}^2 + \overline{v'}^2}{2}, \tag{1}$$

where u' and v' represent the fluctuations of the currents, and the overbar denotes their time-average conditions.

It reveals contrasting levels of mesoscale activity in the tropical South-East Atlantic Ocean, characterized by highest energy levels ($\sim$500 cm^{2}s^{-2}) to the north of 5°S, closer to the coast (inshore); lowest energy levels ($\sim$25 cm^{2}s^{-2}) between 7°S and 25°S, mostly confined offshore, over the central Angolan Basin; and relatively high energy levels ($\sim$200 cm^{2}s^{-2}) to the south of about 25°S, over the northern Cape Basin, restricted to the off-shelf environment (Figure 2a). Note that the lowest energy levels in this latitudinal band covering almost the entire coast of Namibia is confined closer to the coast (inshore), setting a nitid contrast to the condition along
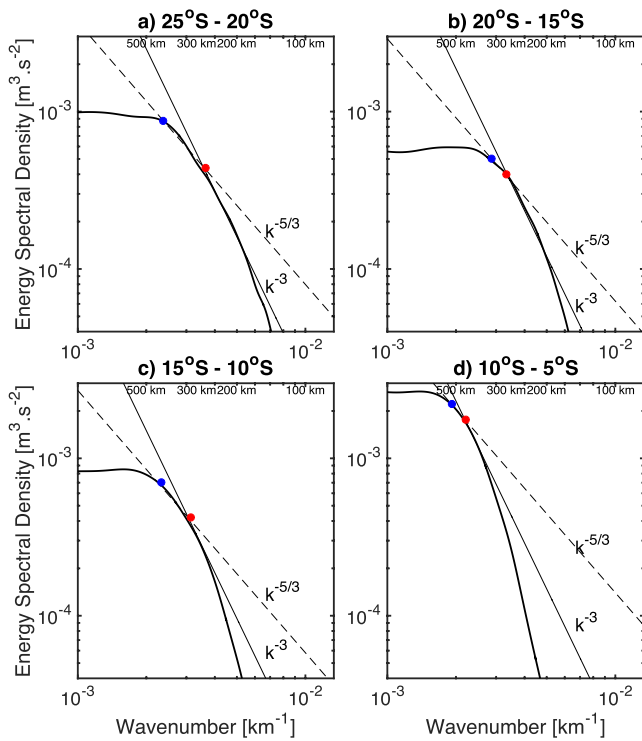
Figure 3. Kinetic energy density spectra [m³s⁻²] as function of wavenumber [km⁻¹], zonally averaged between 8°W and 12°E, distributed along four latitude bands: (a) 25°S–20°S, (b) 20°S–15°S, (c) 15°S–10°S, and (d) 10°S–5°S. Straight lines represent Kolmogorov power laws for turbulence, whereby the solid line portrays k^{-3} transfer, and dashed line represent $k^{-5/3}$ transfer. The spectra are derived from AVISO, averaged over 1993–2017 in bins of 5°Latitudinal bands. The red dots on the figure unveils the scale of energy and enstrophy injection. Their estimated wavelengths (λ) are nearly 275 km at 25°S–20°S, 300 km for 20°S–15°S, 350 km for 15°S–10°S, and 454 km for 10°S–5°S. The blue dots correspond to Rhines scale where eddies are expected to radiate as waves (inverse cascade is halted). Their corresponding λ are nearly 420 km at 25°S–20°S, 350 km for 20°S–15°S, 450 km for 15°S–10°S, and 520 km for 10°S–5°S.

the Angolan coast. The condition along the Angolan coast resembles the intrusion of warmer equatorial waters through the Angola Current, as documented by Rouault et al. (2007). On the other hand, the condition along the Namibian coast resembles the cooler condition of the Benguela Current, and it's upwelling regime. The transition region between the Benguela Current and the Angola Current reveals a frontal system, commonly known as the Angola-Benguela Frontal zone. Perhaps one of the most important take home messages worthy to mention is that the overall inspection of the MEKE along the coastal zone, as depicted in Figure 2a, is the occurrence of three latitudinal zones of contrasting mesoscale activity (Colas et al., 2012).

An attempt to identify the underlying processes in these latitudinal zones was carried out as shown in Figures 2b and 2d. They present the variability of the sea-surface height (SSH), computed as root mean square (RMS) of daily SSH, spanning from 1 January 1993 to 31 December 2017. In Figure 2b, the seasonality is included, while it has been removed in Figure 2c to filter-out variability related to seasonal fluctuations of the oceanic surface currents. The seasonality was removed by extracting the seasonal anomalies as in Marchesiello et al. (2003) and Penven et al. (2005), in our case with reference to the four austral seasons. The difference between the seasonal and non-seasonal fields is presented in Figure 2d, expressed in percentage (%). It highlights the importance of the seasonal variability compared to flow variability at higher frequencies. Notice that in some places it accounts for about 55% of the signal. The presence of near circular geometrical features amid some zonally elongated structures, more notable to the south of 15°S, hypothesize a prevailing occurrence of mesoscale eddies in a wave dominated environment (Quartly et al., 2006; Willett et al., 2006).

We keep in mind that a broad spectrum of mesoscale oceanic variability exist, hence waves and nonlinear eddies of different scales can co-occur (Wunsch, 2000), and indeed overlap (Tulloch et al., 2009). Furthermore, mesoscale eddies can propagate with phase-speed of the linear baroclinic Rossby waves (McWilliams & Flierl, 1979). To re-inforce our analysis, we have inspected the eddy kinetic energy density spectra along the coast across different latitudinal bands.

3.1. Energy Density Spectra

Figure 3 shows zonal energy density power spectra from geostrophic velocities computed using daily satellite altimetry data set over the period between 1993 and 2017. The zonal distance spans from 8°W to 12°E, and the meridional distances are averaged over 5°across four latitudinal bands, from 25°S to 5°S.

The southernmost band spans between 25°S and 20°S, and it lies in the northern sector of the Cape Basin (Figure 3a). The central band spans from 20°S–15°S to 15°S–10°S, which encompasses the ABFZ (Figure 3b), and the central Angola Basin (Figure 3c). The northernmost band spans from 10°S to 5°S, and it lies within the northern sector of the Angola Basin (Figure 3d).

Patterns observed in Figure 3 are typical for 2D geostrophic turbulence on a β-plane (Vallis, 2006). Consistent with features shown in Figure 2, the energy level in Figure 3 shows much larger values in the northern Angola Basin (Figure 3d) and in the northern Cape Basin (Figure 3a), the former being the highest. Understandably its proximity to the equator would greatly contribute toward this signal, and can be attributed to the equatorial instabilities, which in this region are known to favor the propagation of Rossby waves (Illig & Bachelery, 2019; Kongue et al., 2017), as also our analysis on critical latitude discussed in the next section appears to suggest. The latter can be attributed to the eddy activity known to dominate the region (Doglioli et al., 2007; Duncombe-Rae

et al., 1996; Hall & Lutjeharms, 2011; Nencioli et al., 2018), as is also corroborated in Figure 2. The lowest energy level has been observed across the latitude band of the ABFZ (Figure 3b).

Inspection of the profiles shown in Figure 3 reveals that at higher wavenumbers, the energy levels are usually dropping off as the abilities to resolve high-resolution levels (higher frequency variabilities) are limited. This may suggest that the derived results are sensitive to the spatial and temporal resolution of the altimetry data.

In 2D turbulence, the intersection between k^{-3} and $k^{-5/3}$ profiles define the break in slope (i.e., red dots in Figure 3), and corresponds to the energy and enstrophy injection forcing scale (Kundu, 1990). Energy is fluxed toward larger scales (lower wavenumber) while enstrophy is toward smaller scales of dissipation (larger wavenumber), where molecular diffusion becomes important (Kundu, 1990; Vallis, 2006). It is evident from Figure 3 that below the break points (i.e., red dots) the spectra follows more closely the theoretical profile of k^{-3} (enstrophy cascade), whereas above the break points, the profiles follow more closely the slopes of $k^{-5/3}$ (energy cascade).

Important to mention that at scales smaller than 100 km, AVISO data set are very dissipative (the energy is much smaller than what would be expected from a direct energy cascade). This is a clear illustration of the low effective resolution of AVISO product. For a wavelength $\lambda = 200$ km, an eddy radius $R = 50$ km is expected.

Notice that for each of the break points, the corresponding wavelengths λ have been specified in Figure 3. It increases equatorward: $\lambda = 275$ km (latitude band 25°S–20°S), $\lambda = 300$ km (latitude band 20°S–15°S), $\lambda = 350$ km (latitude band 15°S–10°S), and 454 km (latitude band 10°S–5°S). Dividing each λ by 4, this corresponds to an expected eddy radii of $R = 68.75$, $R = 75$, $R = 87.5$, and 113.5 km, respectively.

In geostrophic turbulence on a β-plane the inverse cascade (upscale energy transfer) is halted at the Rhines scale (L_R), where eddies are expected to radiate as waves (Kundu, 1990; Rhines, 1975). This can be seen by the blue dots on the spectra in Figure 3, which can be also visually traced by a change in slope of the energy density spectra. They correspond to wavelengths of $\lambda = 420$ km for Cape Basin (Figure 3a), $\lambda = 350$ km for ABFZ (Figure 3b), $\lambda = 430$ km in central Angola Basin (Figure 3c) and $\lambda = 520$ km in the northern Angola Basin (Figure 3d). These correspond to eddy radii $R = 105$ km, $R = 87.5$ km, $R = 107.5$ km, and $R = 130$ km respectively.

Notice that above the break points, the slopes of the density spectra are flattered toward larger scales, thus deviating from $k^{-5/3}$ profile, suggesting a regime change. Notice that in Figure 3d the profile is somehow different from the other profiles. As can be perceived, it is closer to the equator, thus other dynamics (such as waves) appears to gain relative importance and the spectrum drifts away from the inertial ranges, that is, large deviation with k^{-3}.

To further investigate our claims of the regime transition, we have computed and inspected the onset of the critical latitude value. The details are presented in Section 3.2.

3.2. Critical Latitude

While investigating regime transition between waves and eddies in a quasi-geostrophic formulation of a two-layer shallow water model, Theiss (2004) computed the metric ratio between the Rhines scale (L_R) and the baroclinic Rossby deformation radius (R_D), $r = \frac{L_R}{R_D}$. For $\frac{L_R}{R_D} > 1$, waves were not able to transfer energy into alternating zonal flows, which then has permitted the emergence of eddies. The opposite occurs for $\frac{L_R}{R_D} < 1$. For $\frac{L_R}{R_D} = 1$ a critical latitude can be determined. Klocker and Abernathey (2014) proposed Theiss (2004) formulation r in a quadratic form:

$$r = \left(\frac{L_R}{R_D} \right)^2 \tag{2}$$

The relationship between L_R, and R_D are shown in Figures 4 and 5-a. The deformation radius is portrayed with black contours and the Rhine scale is depicted in red color. Here R_D is computed from hydrographic data from WOA18, obtained by solving the Sturm-Liouville eigenvalue problem. Comparison against global data set published by Chelton et al. (1998), freely available from http://www-po.coas.oregonstate.edu/, showed similar results. However, the use of WOA18 provides better representation, especially over the continental shelf, due to its relatively higher resolution of the data set.

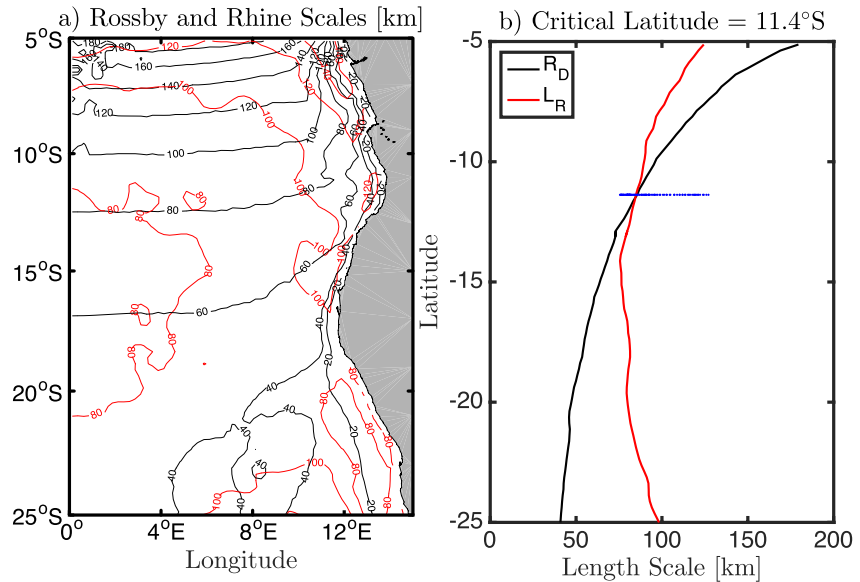$$R_D = \int_{-h}^{0} \frac{N}{|f|\pi} dz. \tag{3}$$

Figure 4. (a) First baroclinic Rossby radius of deformation (black: $R_D = \int_{-H}^{0} \frac{N}{|f|\pi} dz$), and the Rhines scale (red: $L_R = \sqrt{\frac{2 \times U_{rms}}{\beta}}$). (b) Zonal averages of R_D, L_R between 0° and 18°E, along 5°S25°S latitude range. The intersection between R_D and L_R, identified by blue horizontal line in Figure 5b, defines the critical latitude occurring 11.4°S.

where $N = \sqrt{-\frac{g}{\rho} \frac{\partial \rho}{\partial z}}$ is the Brunt-Väisälä stratification frequency, and ρ is oceanic potential density computed using the equation of state (Jackett & McDougall, 1995), vertically integrated from a depth level h, and f is Coriolis parameter.

The Rhines scale was computed following Rhines (1975)

$$L_R = \sqrt{\frac{2 \times U_{rms}}{\beta}} \tag{4}$$

where β is the meridional gradient of the Coriolis parameter, and U_{rms} is the eddy rotational speed, estimated from EKE, as in Klocker and Abernathey (2014), expressed as $U_{rms} = \sqrt{2 \times EKE}$.

Figure 4a shows the distribution of L_R (red contours) superimposed on R_D (black contours). It is notable that both length scales grow equatorward, with R_D ranging from 40 km in the south to 150 km in the north; and L_R ranging from 80 to 120 km, without a specific spatial pattern. The regions of interest are the intersection between the scales of same magnitude value (i.e., where $R_D = L_R$). Figure 4a suggests the intersections between scales of 80 km, slightly offshore, evident at about 12.5°S, between 1°E and 8°E; and for scales of 100 km, closer to the coast, near 10°S, 10°E. These results suggest that a critical latitude lies within the latitudinal band between 10°S and 12.5°S. By zonally averaging the results presented in Figure 4a, along all latitudinal distance, we have been able to establish the overall critical latitude point, occurring at 11.4°S (Figure 4b).

In their study Klocker and Abernathey (2014) have determined r in the eastern Pacific and found a wave-eddy transition to occur around 18°S. Numerical model simulations by Theiss (2004) found a critical latitude at 9°S when a constant eddy velocity of 43 cm.s^{-1} was used, and 18.5°S when a velocity value of 10 cm.s^{-1} was used. In a domain similar to our in this study, Penven et al. (2005) on the basis of a regional ocean circulation model configured to the Peru Current system in the Pacific Ocean found a critical latitude occurring at about 3°S. One should note that the on-set of a critical latitude is more sensitive to the velocity field than β itself.

Following Klocker and Abernathey (2014), we have computed and mapped the logarithm of parameter r (i.e., $\log(r)$) and presented in Figure 5a. The isolines of 0 and 1 are indicated by the black contours. As expected by the theoretical prediction for $\log(r) > 1$, the emergence of eddies can be expected. On the other hand, the tendency for their suppression will be manifested for $\log(r) < 1$. Our inspection in Figure 5a suggests that dominant presence of mesoscale eddies can be expected in areas to the east and south of the contour of $\log(r) = 1$.
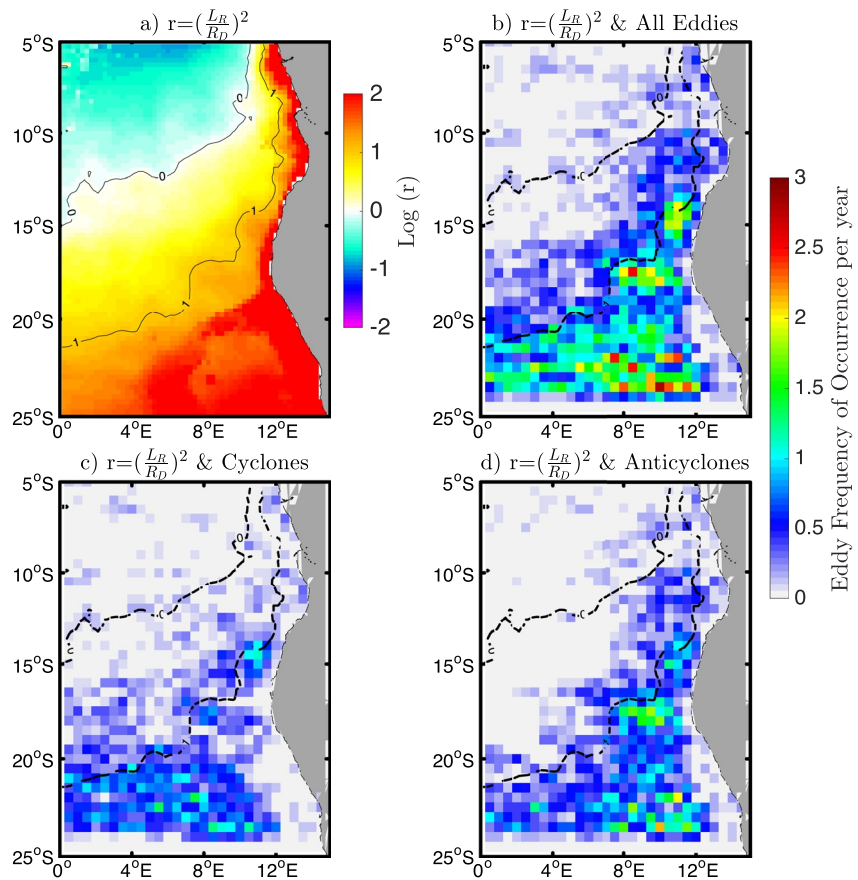
Figure 5. Horizontal length scales expressed in term of (a) log(r), where $r = (\frac{L_R}{R_D})^2$, with isolines of 0 and 1 indicated by black contours. L_R is the Rhines scale (Rhines, 1975), and R_D is the first baroclinic Rossby radius of deformation, obtained by solving the Sturm-Liouville eigenvalue problem, using hydrographic data from WOA18. The background shading from (b to d) represent the eddies frequency of occurrence per year, estimated in boxes with bin size of $0.5° \times 0.5°$, for the all tracked eddies from 1 January 1993 to 31 December 2017. (b) is the total eddies (i.e., combined cyclones and anticyclones). (c) Cyclonic and (d) anticyclones. In all panels, the black dashed contours represents log(r).

An interesting pattern can be observed: to the south of about 20°S, eddies can be expected almost everywhere, whereas to the north of this latitude, eddy dominance is gradually confined toward the coastal zone (Figure 5a). To consolidate these claims, we have run the automatic eddy identification and tracking algorithm (Halo et al., 2014) in the whole domain as described in Section 3.3.

3.3. Eddies

The algorithm for the eddy detection was applied on MADT for the period spanning from 1 January 1993 to 31 December 2017. The eddies were searched within the domain shown in Figure 1, which covers the whole tropical South-East Atlantic Ocean, between 10°W–20°E, and 6°N–25°S. It encompasses the Guinea Basin to the north, the Angola Basin in the center, and the northern sector of the Cape Basin to the south. Prominent bathymetric structures in the area include the North-South oriented Mid-Atlantic Ridge to the west, the North-East section of the Walvis Ridge to the southeast, and the North-East oriented Guinea Sill (Figure 1).

3.3.1. Eddy Statistics

Eddies of both polarities were detected, and their frequency of occurrence per year as presented in Figure 5b was determined using the method implemented in Halo et al. (2014), in bins/pixels of 0.5°. Interestingly, similar analysis performed by H. M. A. Aguedjou et al. (2019) provides very comparable results in spite being computed in bins of $0.2° \times 0.2°$.

It is important to note that daily satellite altimetry maps of absolute dynamic topography (spatially gridded at 1/4°, for the period spanning from 1 January 1993 to 31 December 2017) are used. The temporal resolution of these altimeter maps, on the other hand, is not daily but typically around 10 days (primarily driven by the T/P and JASON precision altimeter repeat cycles). The frequency of occurrences is therefore related to the altimeter observations (and corresponding map production) at this repeat cycle, rather than to the daily updated maps. The merging of additional altimeters at their repeat cycles may not alter this much, maybe at best to 1 week. This must be properly clarified.

The black contours in Figure 5 also indicate $\log(r) = 0$ and 1. Consistent with the theoretical prediction (Figure 5a), higher density of eddies are observed in regions where $\log(r) > 1$ (Figure 5b). A sharp reduction in their occurrence is evident around 10°–11°S, decreasing significantly to the north of this latitude. Three regions of high eddy occurrence (potential hotspots of eddy formation in the region) can be defined. The highest is located between 20° and 25°S, which is the northern sector of the Cape Basin, with a rate of about three eddies per year, observed across a relatively larger spatial extension (Figure 5b). This is consistent with results from H. M. A. Aguedjou et al. (2019) who found an annual frequency of four eddies per year (See their Figure 2a). The second region is located between 15° and 20°S, centered at about 17.5°S, 8°E. This localized region coincides with the position of the ABFZ. The third region lies between 13° and 15°S, and is relatively less intense among all. An occurrence of about two eddies per year is suggested (Figure 5b). The position appears to coincide with the location of the southern most extension of the Angola Current, where it deflects toward offshore (see Figure 2a). Unfortunately this level of details is not easily identifiable in the results from H. M. A. Aguedjou et al. (2019) and H. Aguedjou et al. (2021), likely due to the mapping approach used in their study, which appears to fail to address small scale domains.

The separation between cyclonic and anticyclonic eddies are presented in Figures 5c and 5d, respectively. Both cyclones and anticyclones show similar distribution pattern, but with relatively higher density for anticyclones (Figure 5d) than cyclones (Figure 5c). The theoretical predictions as depicted by the distribution of $\log(r)$ values are remarkably well supported.

The individual eddy generation sites and their trajectories are shown in Figure 6 (left panels). They show the spatial and temporal distribution of the eddies during different stages of their lives. It also highlights the generation sites (bold dots), pathway trajectories of their propagation (track lines), and sites of decay or possibly disappearance from the sea surface (end of the track lines). For visualization purposes only eddies with a life-time of and greater than 7, 30, and 120 days have been presented (Figure 6). As such, they provide a comprehensive holistic view of the spatial/temporal occurrence and predominance over the entire tropical South-East Atlantic Ocean, during the past 24 years. It is important to remember that the marks for the eddy's centre position which represents their generation sites in Figure 6 (left panels) have been enlarged to allow also a better visualization. However, when several generation sites overlap, or are in close proximity with one another, they may appear to reach the coastline. As indicated earlier, the accuracy of the altimetry MADT data used to identify and track the eddies is up to 10–15 km close to the coast (Pujol et al., 2016).

The sequence of the eddies life-stages shown in Figure 6 (left panels, from the top to the bottom) provide the corresponding totals of 1,642, 435, and 44 structures respectively. Their relative proportions in terms of cyclonic and anticyclonic are presented in Table 1. The estimates were obtained by counting the number of all eddies within the domain in each time-frame.

For each period presented in Figure 6, a corresponding histogram of the eddy occurrence (in percentage %) by size (radius in km) is shown in the right panel. The dark-gray (light-gray) bars denote cyclonic (anticyclonic) eddies respectively. Because of the spatial limitations of the altimetric grid resolution of 1/4° × 1/4°, our analysis of the detected mesoscale eddy structures have discarded eddy features with radii smaller than 50 km, to prevent any potential influence of data artifacts. This may explain why H. M. A. Aguedjou et al. (2019) found slightly more eddies in this region, because they have included features up to 30 km radii.

As can be perceived from the total count (1,642), eddies do occur in great number in the tropical South-East Atlantic Ocean, however, they are short-lived. Results (not shown) have revealed that during the first 14 days of their lifetime about 40% of them disappeared. Over the first 30 days, about 73.5% of the total number of eddies have vanished (Figure 6b). This suggests that the eddy field is strongly suppressed, especially between 5°S and 5°N. likely by the enhanced wave activity of the background flow which have been documented in many studies in this region (Grodsky & Carton, 2006; Illig & Bachelery, 2019; Kongue et al., 2017; Ostrowski et al., 2009;
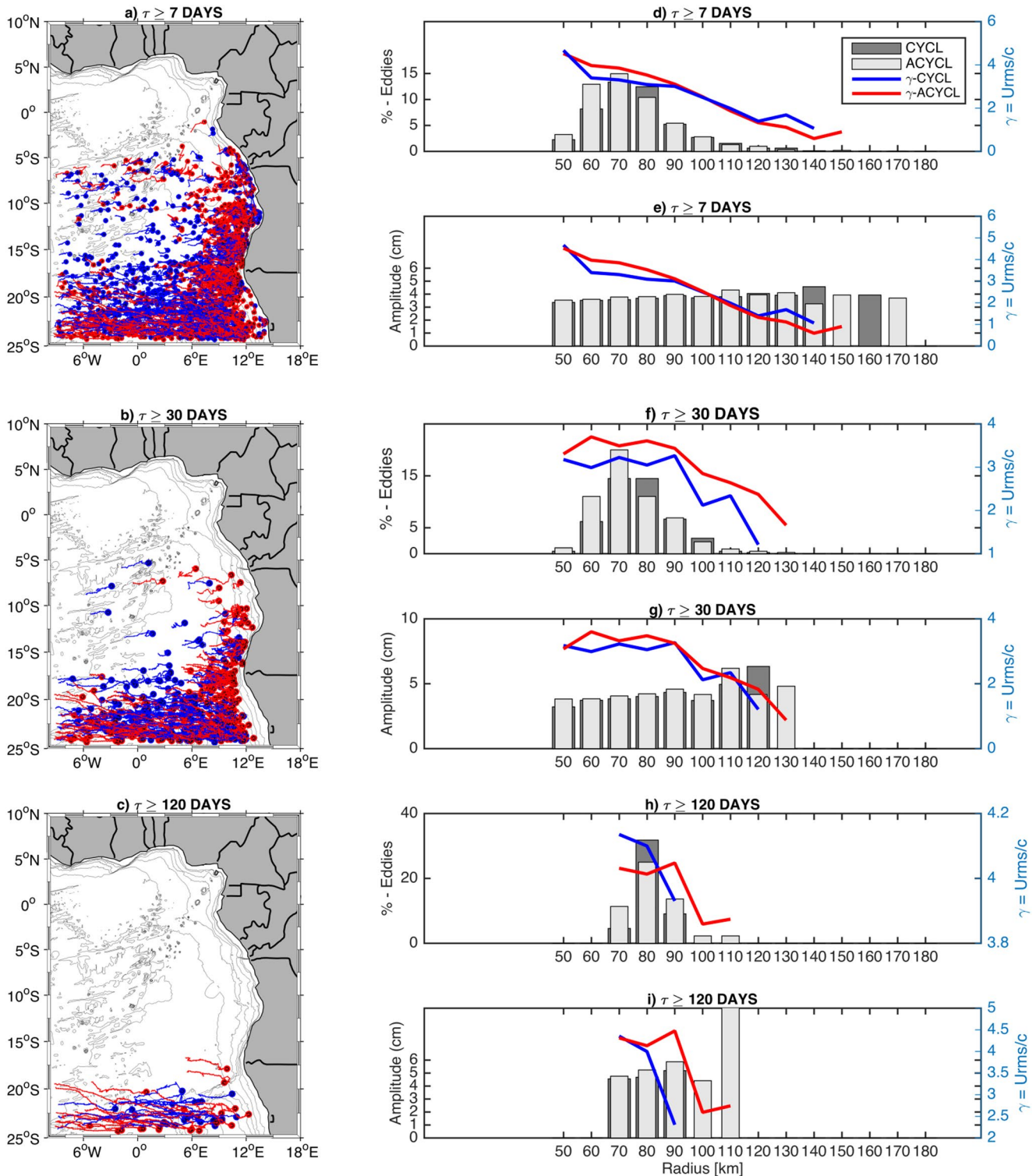
Figure 6. Panels (a–c) show the eddy generation sites (bold dots), trajectories of their propagation (continuous tracks), and positions of decay (end of the tracks), during different stages of their lifespans (i.e., 7, 30, and 120 days respectively). Blue represents cyclonic eddies and red anticyclonic. The background contours show the isobaths of 200, 500, 1,500, 2,500, 3,500, and 4,500 m. Panels (d–i) show the corresponding density and amplitude distribution of the eddies as function of their radii. Cyclones are represented by dark gray and anticyclones by light gray. In each panel the eddies nonlinearity parameters (γ) are represented (bue line for cyclones and red line for anticyclones). The eddies were tracked over a time period between 1 January 1993 and 31 December 2017. In view of the limited altimetric grid resolution ($1/4° \times 1/4°$), eddy structures with radii smaller than 50 km have been discarded from the analysis to prevent any potential data artifacts.

Table 1
Eddy Statistics and Mean Eddy Properties Estimated Within 10°W–18°E and 10°N–25°S

No days	Properties	Cyclones	Anticyclones
	N_{eddies}	783	859
	L (km)	155.74 ± 34.48	149.60 ± 33.75
7	η (m)	3.69 ± 0.59	3.79 ± 0.76
	x (km)	113 ± 145.39	112 ± 148.75
	τ (days)	27 ± 38	29 ± 35
	K (m²s⁻²)	55.48×10^{10}	75.59×10^{10}
	γ	3.02	3.37
	N_{eddies}	200	235
	L (km)	154.37 ± 22.90	159.56 ± 26.13
30	η (m)	3.96 ± 0.70	4.16 ± 0.90
	x (km)	251.17 ± 228.73	243.98 ± 230.03
	τ (days)	67 ± 58	66 ± 49
	K (m²s⁻²)	2.98×10^{10}	4.2×10^{10}
	γ	3.02	3.27
	N_{eddies}	20	24
	L (km)	162.03 ± 11.54	163.89 ± 20.64
120	η (m)	4.77 ± 0.90	5.55 ± 1.75
	x (km)	777.09 ± 369.20	755.03 ± 383.79
	τ (days)	204 ± 94	188 ± 57
	K (m²s⁻²)	0.3×10^{10}	0.55×10^{10}
	γ	4.08	4.08

Note. The estimates were made from altimeter-based eddy detected from 1 January 1993 to 31 December 2017, at different stages of their lifespan (τ), namely, 7, 30, and 120 days. The other terms in the table are: total number of eddies (N_{eddies}), eddy diameter (L), eddy amplitude (η), eddy traveling distance (x), eddy surface integrated energy (K) and eddy nonlinearity factor (γ).

Schouten et al., 2005); which are in agreement with our results presented in the previous paragraphs.

Notably there are slightly more cyclonic eddies generated offshore, whereas the anticyclonic eddies appear more confined to the coast. Analysis by Meeuwis and Lutjeharms (1990) indicated more prevalence of cyclonic eddies than anticyclonic eddies. The latter were generated mostly between 12° and 16°S along the longitude of 9°E, whereas the former have dominated between 13° and 16°S and 3°–5°E (Meeuwis & Lutjeharms, 1990). In the present study, in contrast, we find on average a prevalence of more anticyclonic eddies during the all life-stages considered (Table 1). This pattern of asymmetry in the altimetric detected mesoscale eddies could be related to the dynamical stability and robustness of anticyclonic eddies having typical scale larger than the local deformation radius, as revealed in global studies of mesoscale eddies (Chelton, Schlax, & Samelson, 2011), as well as in regional studies such as that in the Mediterranean Sea (Stegner et al., 2021). Stable anticyclonic eddies tend to remain more coherent within a turbulent flow, and are more robust to an external strain and shear than their counter-parts (Graves et al., 2006).

3.3.2. Eddy Nonlinearity Factor

The blue and red profiles overlaid in each histogram presented in Figure 6 show the eddy nonlinearity factor (γ) proposed by (Chelton et al., 2007), for cyclonic and anticyclonic eddies respectively. It is expressed as the ratio between the eddy rotational speed (U_{rms}) and eddy advective speed (c),

$$\gamma = \frac{U_{rms}}{c} \tag{5}$$

It gives an insight on the ability of an eddy to conserve its coherent structure, and trap material in it's core. When $\gamma > 1$ the eddy is highly nonlinear and is able to trap material, whereas when $\gamma < 1$ the eddy is weakly nonlinear and unable to retain material within its core over time (Chelton et al., 2007; Chelton, Schlax, & Samelson, 2011).

The magnitudes of γ as a function of the eddy radii, R (km) at various stages of the eddies lifespan (days) (Figure 6), reveal that almost all the identified mesoscale structures were nonlinear. Exceptions were observed at 7 days for anticyclonic structures with radii-scale R larger than 130 km and cyclones with radii R larger than 150 km, as can be seen in the histogram of Figure 6a. They amount in total to 7 mesoscale structures, being 1 cyclone and 6 anticyclones, which corresponds only to 0.43% of the 1,642 identified structures. These findings confirm the robustness of the mesoscale eddy detection method used in this study, with successful score rate of about 99.57%. It might also suggest that possibly Rossby waves were masked as eddies (Paulo & Sato, 2015). This could explain why they have been identified as an eddy in the first place. Or perhaps, instabilities were favoring an upscale cascade of energy from eddies to waves (Klocker & Abernathey, 2014). The claims are further supported in view of the dominant scales, whereby Rossby waves (∼ 200 km and more) are usually found at the domain of larger spatial/temporal scales, in contrast to mesoscale eddies (order of ∼100 km).

Looking at the prevailing eddy radii evolution in time in the histograms (Figures 6d, 6f, and 6h), and relating it with the spatial and temporal distribution maps of the eddies presence (Figures 6a–6c), it becomes apparent that the wave-like structures only lived less than 30 days. In fact results not shown suggests only 14 days.

The histograms in Figures 6d, 6f, and 6h, also shows that the size distribution is nearly bell-shaped, regardless of their lifestages, essentially ranging between $R = 50$–130 km radii, with most predominant peak centered between $R = 70$–80 km, a length-scale which is consistent with vigorous regime of geostrophic turbulence through baroclinic instabilities within the latitude range of the study region. The sizes of the eddies assessed here are similar with those inspected by H. M. A. Aguedjou et al. (2019), in spite differences on the imple-
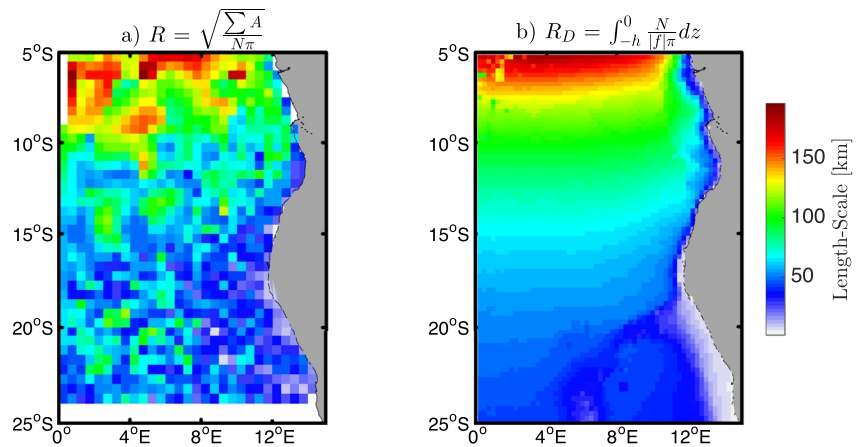
Figure 7. (a) Frequency of eddy radii size occurrence in box sizes of $0.5° \times 0.5°$, computed from eddies identified by the automatic algorithm from 1 January 1993 to 31 December 2017, for all eddies with a lifespan of 7 days and greater, in the South-East Atlantic Ocean. (b) First baroclinic Rossby radius of deformation computed using WOA18 data set.

mented eddy identification algorithm. This could be related to the fact that both studies have used the same altimetry data set, nearly over the same time period, being H. M. A. Aguedjou et al. (2019) up to 2015 (only 2 years shorter).

Interestingly variabilities at the timescale of ~14 days in this region has been related to equatorial wave energy transmitted as Coastal Trapped Waves along the coasts of Congo and Angola. This in turn may imprint anomalous variability in SSH captured by satellite altimetry, that dissipates the coherence between equatorial oscillations and variabilities of the SSH anomalies (Illig & Bachelery, 2019).

3.3.3. Eddy Mean Properties

We have investigated the following eddy mean properties: size, amplitude, lifetime, traveling distances, kinetic energy and nonlinearity parameter (Table 1). The equivalent eddy mean radii R is estimated using the relation proposed by Souza et al. (2011):

$$R = \sqrt{\frac{\sum A}{N \pi}} \tag{6}$$

where A is the eddy's surface area, assumed to have a circular geometry, and N is the total number of eddies. Its geographical distribution is presented in Figure 7a, in terms of frequency of radii occurrences in boxes with a bin size of $0.5° \times 0.5°$.

Table 1 shows no clear diameter (L (km)) distinction between cyclonic and anticyclonic eddies. In some cases L of the cyclones were larger than the anticyclones, while in other cases it was the opposite. On the other hand, a more coherent pattern was observed for the amplitudes (η (m)), estimated using the criteria implemented by Chelton, Schlax, and Samelson (2011), based on the difference between the maxima and minima extrema of the eddy's surface height. We found a moderate and significant correlation between eddy amplitude and their lifespan (τ (days)) ($\mathbf{r} = 0.59$, $p < 0.05$). Throughout, the overall mean amplitude of the anticyclonic eddies were higher than their counter-parts (Table 1). The same was true for their standard deviation, which suggests that they present relatively higher levels of variability. However, when the eddies are clustered per sizes, it becomes obvious that there are specific scales at which the amplitude of the cyclonic eddies are higher than the anticyclonic (e.g., at 140, 160 km in Figure 6e; 120 km in Figure 6g).

Table 1 shows that cyclonic eddies in general traveled relatively longer marginal distances (x (km)) than the anticyclonic. The traveling distance has been estimated as the maximum eddy displacement relative to their origins. The lifespan was determined as the time-difference between the dates when the eddies were first identified and last observed (Halo et al., 2014). Evidently the traveling distances increased with increasing eddy lifespan (Table 1), with a strong and significant correlation coefficient ($\mathbf{r} = 0.90$, $p < 0.05$). It is likely that the observed increase in eddy traveling distance with lifespan is related to the increase of their nonlinearity (γ) over time (Table 1). A strong correlation was observed between eddy lifespan and nonlinearity ($\mathbf{r} = 0.81$, $p < 0.05$).
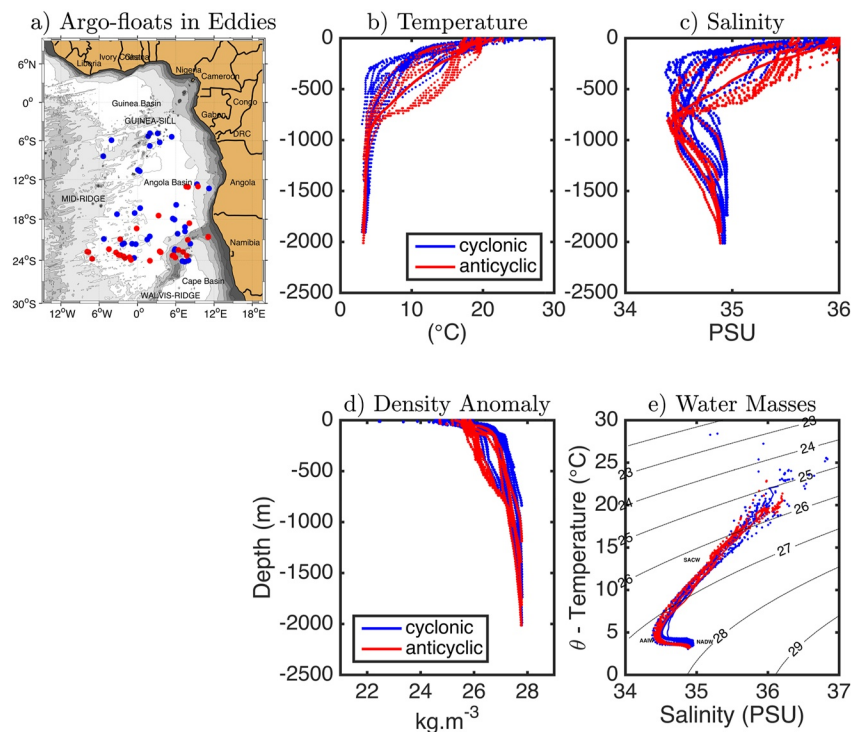
Figure 8. (a) Hydrographic properties in Angola and northern Cape Basins, extracted from Argo-floats trapped within the mesoscale eddies identified from satellite altimetric maps from August 1997 to 31 December 2017. Vertical profiles of (b) temperature, (c) salinity, (d) density anomaly and (e) T/S diagram. For all panels blue color denotes cyclones and red color anticyclones.

The spatial and temporal distribution of the eddy field observed in the timeseries (Figure 6-a,b,c) indicates that the eddies formed in the southern parts of the domain (close to the subtropics) have a relatively longer life expectancy than those formed in the north. These results appear somehow consistent with those presented by H. M. A. Aguedjou et al. (2019). See their Figure 2d. In addition, both Table 1 and the histogram plots (Figure 6), shows a consistent southward increase of the nonlinearity parameter as function of the eddy radii (Figures 6d, 6f, and 6h).

Looking at the spatial distribution depicted in Figure 7a, it becomes apparent that larger eddies ($R > 130$ km) are mostly generated to the north of 10°S. It is also evident that the eddies sizes increase from the coast toward the offshore environment, regardless of their latitudinal bands. The overall distribution of the eddy radii increases equatorward, consistently with the first baroclinic Rossby radius of deformation (Figure 7b). One may argue that the sizes of the observed eddies are controlled by the deformation radius, as expected in baroclinic mesoscale turbulence.

3.4. Eddies With Argo Profiles and Satellite Derived Ocean Color

3.4.1. Water Masses

To assess the hydrographic properties in the eddies through the water column, we have used Argo-floats which were identified within the eddies, as described earlier in Section 2.3.1. Their spatial distribution is shown in Figure 8a, where the Argo-floats in cyclonic eddies is represented in blue, and in anticyclonic eddies is represented in red.

Unfortunately only a handful of Argo-floats are seen to circulate in the region, making it difficult to draw a more conclusive information about the eddies vertical structure in the upper 2,000 m (e.g. maximum profiling depths). Both individual and domain averaged vertical profiles of temperature (Figure 8b), salinity (Figure 8c), density (Figure 8d), and the water masses (Figures 8e and 8g) are shown.

Looking at the vertical profiles of temperature and salinity (Figures 8b and 8c), it can be inferred that the anticyclonic eddies on average have a deeper thermocline and halocline structure than the cyclonic edies. Larger dispersion between the individual profiles observed mostly in the upper 800 m may suggest that the eddy variability is more intense in the upper ocean. The corresponding density structure (Figure 8d) also shows a more variable profiles in the upper 800 m, both in cyclones and anticyclones. The profiles also suggest a clear difference in the composition structure between about 200 and 800 m. This may suggest the presence of eddies from different geographical origin within the South Atlantic Basin, which may transport different water masses. In fact analysis of temperature/salinity (T/S) diagram (Figure 8d) indicate the fresher signal in anticyclones to be related with the trapping of Antarctic Intermediate Depth (AAIW), while the structure below 1,500 m to be linked with North Atlantic Deep Water (NADW), as measured in-situ and documented by Stramma and England (1999). Stramma and England (1999) characterizes the AAIW as structure with isopycnal of 27.1 (kg m^{-3}) in the tropics and 27.05 (kg m^{-3}) in the subtropics, ranging from 500 to 1,200 m in the tropics and 600–1,400 m in the subtropics.

On the other hand the structures with similar patterns in both cyclone and anticylones across the thermo/halocline layers suggests the presence of the South Atlantic Central Water (SACW), known to circulate in the tropics via the South Equatorial Current, in depths between 100 and 500 m, and exhibiting a nearly straight line in the T/S diagram (Stramma & England, 1999).

3.4.2. Chlorophyll-a

To assess the eddies potential to influence the local biology, we have mapped the chlorophyll-a distribution trapped within the altimetric derived mesoscale cyclonic and anticyclonic eddy structures (left panels in Figures 9a and 9b).

Subsequently we have inspected the relationship between the eddy's properties, such as size and rotational speed, against the concentrations of chlorophyll-a. In addition we have superimposed the eddy's nonlinearity parameter γ as computed by Chelton et al. (2007). To relate the information with the strength of the dominant mesoscale process, as defined earlier in different spectral bands, we have performed the analysis in different geographical latitudinal bands, namely, northern, central and southern Angola Basin respectively (right panels in Figure 9). As already indicated, a nonlinearity parameter greater than 1 ($\gamma > 1$) is commonly used as a proxy of the ability of an eddy to trap material in its interior (Chelton et al., 2007; Chelton, Gaube, et al., 2011; Early et al., 2011). Inspections of γ based on eddies with a lifespan of 7 days and longer presented in Figure 6a, reveals that 99.57% of all observed eddies were highly nonlinear.

When the concentrations of chlorophyll-a were clustered according to the eddies radii, on an increment of every 10 km, starting from 50 km as shown in Figures 9c, 9e, and 9g, it becomes apparent that regardless of their geographical band, the concentrations of chlorophyll-a also follows a near normal distribution, skewed to the right (toward the larger eddy structures). Overall, Figures 9c, 9e, and 9g resemble the eddy density distribution presented in histograms of Figure 6. The peak of chlorophyll-a concentration in the cyclones occurred at 70 km radius, while the anticyclones were at 80 km in the northern Angola Basin. The opposite was observed in the central Angola Basin. In the southern Angola Basin, the chlorophyll-a concentrations peaked at 60 km radius for anticyclonic eddies and 70 km radius for cyclones. Overall the concentration of the chlorophyll-a were mostly found in eddies with radii between 60 and 80 km, which are typical scales for oceanic surface geostrophic baroclinic turbulence. The amount of chlorophyll-a concentrations within this eddy radii range decreased equatorward. Several studies have investigated the role of oceanic turbulence on chlorophyll-a distribution (Chelton, Gaube, et al., 2011; Dufois et al., 2014; Gaube et al., 2013; José et al., 2014; Lévy et al., 2012; Stramma et al., 2013). Unfortunately in this study the lack of chlorophyll-a data through the water column makes it difficult to assess the exact physical mechanisms driving the enhanced concentration patterns observed in Figures 9a and 9b. Nevertheless, a dominant pattern is evident: Higher concentrations of chlorophyll-a were observed in anticyclonic than in cyclonic eddies. While this seems contrary to the general theory stating that cyclonic eddies are more productive than anticyclonic because of the upwelling phenomena inside of cyclonic motions (McGillicuddy et al., 1998), our results are consistent with results presented by Dufois et al. (2016). They have shown that this general theory is not sustained for a majority of eddies within the subtropical oceanic gyres (Dufois et al., 2016). They argue that the predominance of higher chlorophyll-a concentrations in anticyclones than in cyclones are related to vertical mixing induced by the eddies (Dufois et al., 2016) (see their Figure 1a).

Here several processes such as ageostrophic dynamics in the eddies including upper layer convergence/divergence, vertical motions and turbulent mixing are certainly influencing the concentration levels of chlorophyll-a.
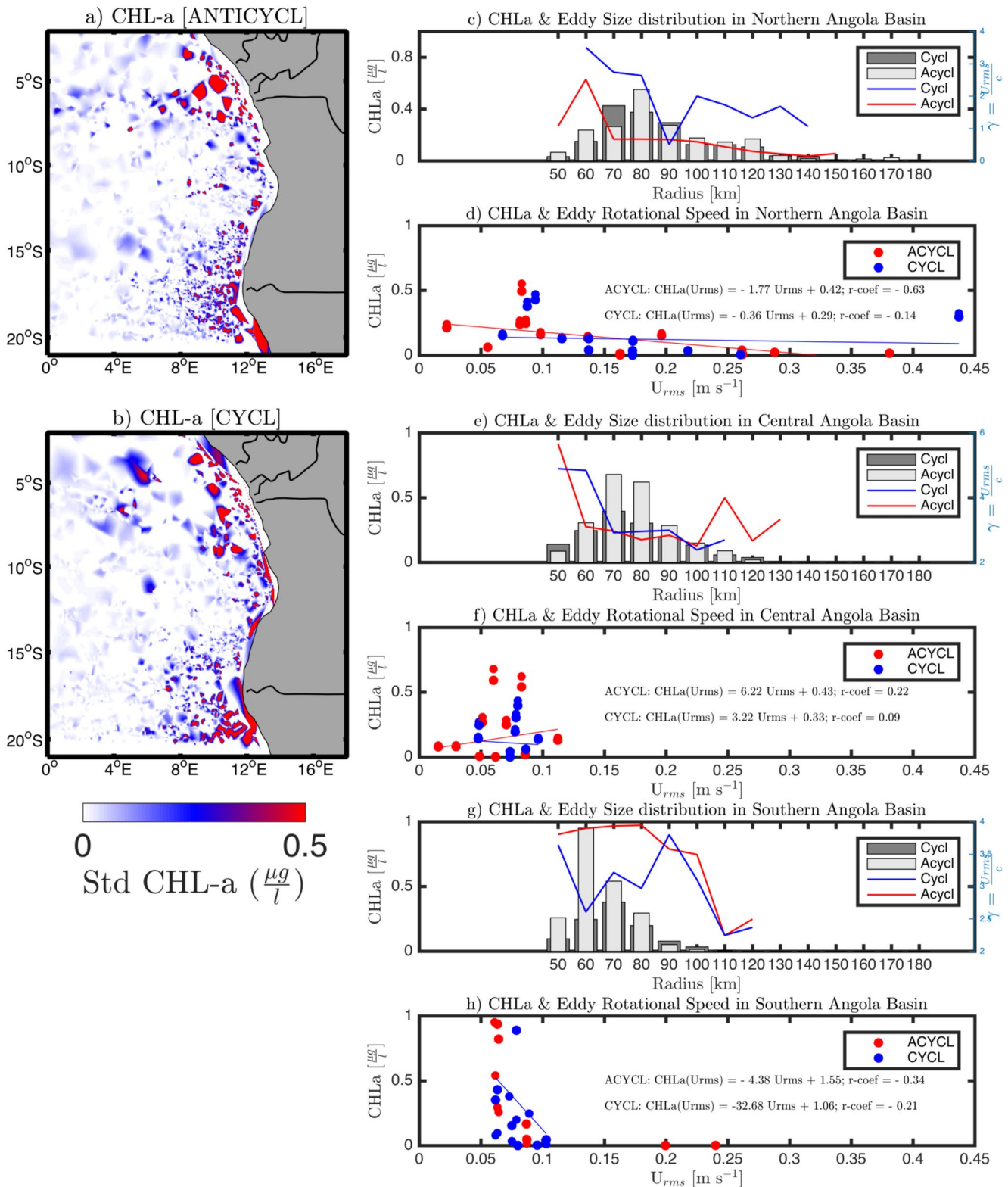
Figure 9.

These will act differently during the eddy development phase (~order of days) versus the later time period (~order of month) when the eddy motion is in a steady state. The dynamics and vertical motion at the rim of the eddies, on the other, will not necessarily reach a steady state. As such they may influence the eddies during all stages of their life-span and be further impacted by the continuously changing wind stress and Ekman interactions. This could impact the chlorophyll-a concentration and thus modify the classical cyclonic versus anticyclonic properties. Lastly, the converging properties of the anticyclonic eddies will also tend to stimulate more accumulation of chlorophyll-a in anticyclonic eddies.

The super-imposed profiles shown in Figures 9c, 9e, and 9g, represent the nonlinearity parameter γ for cyclones (blue) and anticyclones (red). Therefore more physical processes can be explored from this parameter, as it reflects a measure of eddy coherent structure, and trapping capacity (Chelton, Gaube, et al., 2011). Overall cyclonic eddies trapping chlorophyll-a had stronger nonlinearity parameter γ than their counterparts in the northern Angola Basin (Figure 9c). In the central Angola Basin (Figure 9e), dominance of the nonlinearity parameter of the cyclones over anticyclones were observed in eddies with radius between 60 and 90 km. In the southern Angola Basin (Figure 9c), the nonlinearity of the cyclones were overall lower than the anticyclones.

Linear regression analysis performed in each latitudinal band indicated above, between the chlorophyll-a distribution and eddy's rotational speed are shown in Figures 9d, 9f, and 9h). For all regions highest concentrations of chlorophyll-a were observed in eddies with rotational velocities ranging between 0.05 and 0.1 m s^{-1}. The decay in chlorophyll-a concentration with increasing eddy rotational velocities as seen in Figure 9d, where a moderate, negative correlation for anticyclonic eddies exists ($\mathbf{r} = -0.63$), may suggest that the chlorophyll-a is mostly confined toward the eddy's center than it's peripheries, where the velocities are generally greater.

4. Conclusions

In this study 24 years of satellite altimetry-derived variations of the sea-surface height in the tropical South East Atlantic Ocean was used to examine the mesoscale flow variability across a wide range of oceanic intermediate length scale (10–400 km) in combination with Argo profiling floats, WOA18 climatology and satellite-derived ocean color data. The following key findings and results have emerged.

Horizontal length-scales of geostrophic mesoscale ocean flows including the first baroclinic Rossby radius of deformation, Rhines-scale as well as eddy radii estimated from eddies tracked using an automatic eddy detection algorithm have been inspected in order to investigate the mesoscale variability and flow regime transition in the tropical South-East Atlantic Ocean.

Analysis of eddy energy spectra density following power laws revealed an equatorward inverse cascade of energy in the region, which appears to limit the growth of mesoscale eddies and favor an evolution of Rossby waves, thus leading to an enhanced reduction of the eddy population in the region, where the ratio between the Rossby and Rhines scales suggested an emergence of a critical latitude at about 11.4°S. We argue that to the best of our knowledge this is the first time that such information has been documented for this region. Therefore these results add value to the local knowledge, and complements the studies of oceanic mesoscale variability conducted in the region.

Eddy census conducted in the region revealed that the eddies lifespan increased polewards. Their lifespan was strongly and significantly correlated with the nonlinearity parameter on the metric defined by Chelton et al. (2007). There was also a strong and significant correlation between eddy lifespan and traveling distances ($\mathbf{r} = 0.90$, $p < 0.05$).

Figure 9. Left panels show the spatial distribution of the standard deviation of the chlorophyl-a distribution derived from satellite ocean color, retrieved inside of altimetric-derived cyclonic (a) and anticyclonic (b) eddies, identified from August 1997 to 31 December 2017. Right panels show both the histograms of standard deviation of the chlorophyll-a concentrations retrieved from satellite ocean color, computed within the mesoscale eddies, as function of the eddies radii (panels c, e, and g), and as function of their rotational speed (panels d, f, and h). In view of the altimetric grid resolution of 1/4° × 1/4°, eddy structures with radii smaller than 50 km have been discarded from the analysis. Panels (c and d) correspond to the region in the northern Angola Basin; panels (e and f) correspond to the central Angola Basin; and panels (g and h) correspond to the southern Angola Basin (i.e., Cape Basin). In all panels: dark gray represents cyclonic eddies and light gray represents the anticyclonic eddies. Superimposed profiles in panels c, e, and g, represent the nonlinearity parameter distribution, with cyclones in blue and anticyclones in red. The superimposed linear trends are shown in panels (d, f, and h), with cyclones represented in blue and anticyclones in red. The linear equations and their correlation coefficients are also presented.

Both cyclonic and anticyclonic eddies have shown similar physical characteristics, featured by a near normal density distribution, with predominant peaks occurring at scales between 60 and 80 km radii. Nevertheless, overall there was an asymmetry on the eddy population, characterized by a dominance of anticyclonic eddies over their counterpart. We hypothesize that this could be related to a more vigorous dynamic stability and robust nature of the anticyclonic eddies than the cyclonic eddies. However, this remains to be tested.

Hydrographic characteristics of the eddies retrieved from Argo profiling floats revealed several distinct water masses trapped within the eddies in the upper 2,000 m, notably, SACW, AAIW, and NADW.

High concentrations of chlorophyll-a were mostly found in anticyclonic eddies than in cyclones, which may suggest that the anticyclonic eddies in this region could be more productive than the cyclones. A dedicated study to consolidate this possibility is recommended.

Data Availability Statement

All the results of this study were generated using open access datasets. The data set are freely available at various institutional databases. The mean dynamic topography (MDT) product (CNES-CLS09) credited to Rio et al. (2011) used to map the streamlines of the flow field, can be accessed by registered users of the website using the link https://www.aviso.altimetry.fr/en/index.php?id=3622. The gridded maps of absolute dynamic topography derived from multi-mission satellite observations is identified with https://doi.org/10.48670/moi-00148, and can be accessed by registed users of Copernicus Marine Environmental Monitoring Service (CMEMS) at the following weblink https://data.marine.copernicus.eu/product/. Temperature and salinity from the world ocean atlas (WOA2018) product used to compute the baroclinic Rossby radius can be found at https://www.ncei.noaa.gov/archive/accession/NCEI-WOA18. The profiling Argo-floats used to assess the eddy hydrography was downloaded from http://www.argodatamgt.org/Access-to-data/Argo-data-selection. The ocean colour used is from Ocean Colour Climate Change Initiative (https://esa-oceancolour-cci.org/). If the weblinks to the data set appears not to work, alternatively copy the link and paste into your web browser. In addition we have centralized all the above listed data products for easy access at zenodo data repository name HALO_JGR_2022JC019050R_DATASET (https://zenodo.org/record/7389301#.Y4nPU2Qzbow), version 1. The automatic eddy identification and tracking algorithm described by Halo et al. (2014), can be found at zonodo software repository name AUTOMATIC EDDY DETECTION AND TRACKING ALGORITHM (http://zenodo.org/record/3862545#.Y4Va83Z-By3A), version 2. The chlorophyll-a within the eddies were estimated using the Nansat algorithm (Korosov et al., 2016) archived at zenodo (https://doi.org/10.5281/zenodo.59998, Licenced under GNU GPLv3, release 0.6.14). All figures were generated using a commercial license of Matlab software from Mathworks, Inc (http://www.mathworks.com), R2021a.

References

Aguedjou, H., Chaigneau, A., Dadou, I., Morel, Y., Pegliasco, C., Da-Allada, C. Y., & Baloitcha, F. (2021). What can we learn from observed temperature and salinity isopycnal anomalies at eddy generation sites? Application in the tropical Atlantic Ocean. *Journal of Geophysical Research*, *126*(11), JC017630. https://doi.org/10.1029/2021JC017630

Aguedjou, H. M. A., Dadou, I., Chaigneau, A., Morel, Y., & Alory, G. (2019). Eddies in the tropical Atlantic Ocean and their seasonal variability. *Geophysical Research Letters*, *46*(21), 12164. https://doi.org/10.1029/2019GL083925

AVISO. (2015). Ssalto duacs user handbook. In *(M)SLA and (M)ADT near-real time and delayed time products. Ssalto. Duacs* (Vol. rev 4). CLS-DOS-NT-06-034.

Beal, L. M., De Ruijter, W. P. M., Biastoch, A., Zahn, R., Cronin, M., Hermes, J., et al. (2011). On the role of the Agulhas System in ocean circulation and climate. *Nature*, *472*(7344), 429–436. https://doi.org/10.1038/nature09983

Biastoch, A., Böning, C. W., & Lutjeharms, J. R. E. (2008). Agulhas leakage dynamics affects decadal variability in Atlantic overturning circulation. *Nature*, *456*(7221), 489–492. https://doi.org/10.1038/nature07426)

Biastoch, A., Lutjeharms, J. R. E., Böning, C. W., & Scheinert, M. (2008). Mesoscale perturbations control inter-ocean exchange South of Africa. *Geophysical Research Letters*, *35*(20), L20602. https://doi.org/10.1029/2008GL035132

Brewin, R. A., Sathyendranath, S., Muller, D., Brockmann, C., Deschamps, P. Y., Devred, E., et al. (2015). The ocean colour climate change initiative: III. A round-robin comparison on in-water bio-optical algorithms. *Remote Sensing of Environment*, *162*, 271–294. https://doi.org/10.1016/j.rse.2013.09.016

Capet, A., Mason, E., Rossi, V., Troupin, C., Faugere, Y., Pujol, I., & Pascual, A. (2014). Implications of refined altimetry on estimates of mesoscale activity and eddy-driven offshore transport in the Eastern Boundary Upwelling Systems. *Geophysical Research Letters*, *41*(21), 7602–7610. https://doi.org/10.1002/2014GL061770

Chelton, D. B., de Szoeke, R. A., Schlax, M. G., Naggar, K. E., & Siwertz, N. (1998). Geographical variability of the first-baroclinic Rossby radius of deformation. *Journal of Physical Oceanography*, *28*(3), 433–460. https://doi.org/10.1175/1520-0485(1998)028<0433:gvotfb>2.0.co;2

Chelton, D. B., Gaube, P., Schlax, M. G., Early, J. J., & Samelson, R. M. (2011). The influence of nonlinear mesoscale eddies on near surface oceanic chlorophyll. *Science*, *334*(6054), 328–332. https://doi.org/10.1126/science.1208897

Chelton, D. B., & Schlax, M. G. (1996). Global observations of oceanic Rossby waves. *Science*, *272*(5259), 234–238. https://doi.org/10.1126/science.272.5259.234

Chelton, D. B., Schlax, M. G., & Samelson, R. M. (2011). Global observations of nonlinear mesoscale eddies. *Progress in Oceanography*, *91*(2), 167–216. https://doi.org/10.1016/j.pocean.2011.01.002

Chelton, D. B., Schlax, M. G., Samelson, R. M., & Szoeke, R. A. (2007). Global observations of large oceanic eddies. *Geophysical Research Letters*, *34*(15), L15606. https://doi.org/10.1029/2007GL030812

Colas, F., McWilliams, J. C., Capet, X., & Kurian, J. (2012). Heat balance and eddies in the Peru-Chile current system. *Ocean Dynamics*, *39*(1–2), 509–529. https://doi.org/10.1007/s00382-011-1170-6

Colberg, F., & Reason, J. C. (2007). A model investigation of internal variability in the Angola Benguela Frontal Zone. *Journal of Geophysical Research*, *112*(C7), C07008. https://doi.org/10.1029/2006JC003920

Djakouré, S., Penven, P., Bourles, B., Veitch, J., & Koné, V. (2014). Coastally trapped eddies in the north of the Gulf of Guinea. *Journal of Geophysical Research*, *119*(10), 6805–6819. https://doi.org/10.1002/2014JC010243

Doglioli, A. M., Blanke, B., Speich, S., & Lapeyre, G. (2007). Tracking coherent structures in a regional ocean model with wavelet analysis: Application to Cape Basin eddies. *Journal of Geophysical Research*, *112*(C5), C05043. https://doi.org/10.1029/2006JC003952

Dufois, F., Hardman-Mountford, N. J., Greenwood, J., Richardon, A. J., Feng, M., Herbette, S., & Matear, R. (2014). Impact of eddies on surface chlorophyll in the south indian ocean. *Journal of Geophysical Research*, *119*(11), 8061–8077. https://doi.org/10.1002/2014JC010164

Dufois, F., Hardman-Mountford, N. J., Greenwood, J., Richardon, A. J., Feng, M., & Matear, R. (2016). Anticyclonic eddies are more productive than cyclonic eddies in subtropical gyres because of winter mixing. *Oceanography*, *2*(5), 1–6. https://doi.org/10.1126/sciadv.1600282

Duncombe-Rae, C. M., Garzoli, S. L., & Gordon, A. L. (1996). The eddy field of the southeast Atlantic Ocean: A statistical census from the Benguela sources and transports project. *Journal of Geophysical Research*, *101*, 11949–11964. https://doi.org/10.1029/95jc03360

Early, J. J., Samelson, R. M., & Chelton, D. B. (2011). The evolution and propagation of quasi-geostrophic ocean eddies. *Journal of Physical Oceanography*, *41*(8), 1535–1555. https://doi.org/10.1175/2011jpo4601.1

Fillipov, E., & Kolesnikov, G. (1971). On origin of southerly components in the system of Benguela Current. *tra*, *33*, 42–49.

Gaube, P., Chelton, D. B., Strutton, P. G., & Behrenfeld, M. J. (2013). Enhanced mid-latitude tropospheric warming in satellite measurements. *Journal of Geophysical Research*, *118*(12), 6349–6370. https://doi.org/10.1002/2013JC009027

Graves, L., McWilliams, J. C., & Montgomery, M. T. (2006). Vortex evolution due to straining: A mechanism for dominance of interior anticyclones. *Geophysical and Astrophysical Fluid Dynamics*, *100–3*, 151–183.

Grodsky, S. A., & Carton, J. A. (2006). Influence of the tropics on the climate of the South Atlantic. *Geophysical Research Letters*, *33*(6), L06719. https://doi.org/10.1029/2005GL025153

Gruber, N., Lachkar, Z., Frenzel, H., Marchesiello, P., M'unnich, M., McWilliams, J. C., et al. (2011). Eddy-induced reduction of biological production in eastern boundary upwelling systems. *Nature Geoscience*, *4*(11), 787–792. https://doi.org/10.1038/NGEO1273

Hall, C., & Lutjeharms, J. R. E. (2011). Cyclonic eddies identified in the Cape Basin of the South Atlantic Ocean. *Journal of Marine Systems*, *85*(1–2), 1–10. https://doi.org/10.1016/j.jmarsys.2010.10.003

Halo, I., Backeberg, B., Penven, P., Ansorge, I., Reason, C., & Ullgren, J. E. (2014). Eddy properties in the Mozambique channel: A comparison between observations and two numerical ocean circulation models. [Software]. Deep-Sea Research, Part II, *100*, 38–53. Zenodo. https://doi.org/10.1016/j.dsr2.2013.10.15

Illig, S., & Bachelery, M. (2019). Propagation of subseasonal equatorially-force coastal trapped waves down to the Benguela upwelling system. *Nature Science Report*, *9*(1), 5306. https://doi.org/10.1038/s41598-019-41847-1

Illig, S., Dewitte, B., Ayoub, N., du Penhoat, Y., Reverdin, G., De Mey, P., & Lagerloef, G. S. E. (2004). Interannual long equatorial waves in the tropical Atlantic from a high-resolution ocean general circulation model experiment in 1981 - 2000. *Journal of Geophysical Research*, *109*(C2), C02022. https://doi.org/10.1029/2003JC001771

Jackett, D. R., & McDougall, T. J. (1995). Minimal adjustment of hydrostatic profiles to achieve static stability. *Journal of Atmospheric and Oceanic Technology*, *12*(2), 381–389. https://doi.org/10.1175/1520-0426(1995)012<0381:maohpt>2.0.co;2

José, Y. S., Aumont, O., Machu, E., Penven, P., Moloney, C. L., & Maury, O. (2014). Influence of mesoscale eddies on biological production in the Mozambique Channel: Several contrasted examples from a coupled ocean biogeochemistry model. *Deep-Sea Research, Part II*, *100*, 100–193. https://doi.org/10.1016/j.dsr2.2013.10.018

Klocker, A., & Abernathey, R. (2014). Global patterns of mesoscale eddy properties and diffusivities. *Journal of Physical Oceanography*, *44*(3), 1030–1046. https://doi.org/10.1175/JPO-D-13-0159.1

Kongue, R., Illig, S., & Rouault, M. (2017). Role of interannual Kelvin wave propagations in the equatorial Atlantic on the Angola Benguela Current system. *Journal of Geophysical Research*, *122*(6), 4685–4703. https://doi.org/10.1002/2016JC012463

Korosov, A., Hansen, M., Dagestad, K., Yamakawa, A., Aleksander, V., & Riechert, M. (2016). Nansat: A scientist-orientated Python package for geospatial data processing. [Software]. Journal of Open Research Software, *4*, e39. Zenodo. https://doi.org/10.5281/zenodo.59998

Kundu, P. K. (1990). *Fluid mechanics* (Vol. 1, p. 638). Academic Press.

Lathuilière, C., Levy, M., & Echevin, V. (2011). Impact of eddy-driven vertical fluxes on phytoplankton abundance in the euphotic layer. *Journal of Plankton Research*, *33*(5), 827–831. https://doi.org/10.1093/plankt/fbq131

Lavender, S., Jackson, T., & Sathyendranath, S. (2015). The ocean colour climate change initiative: Merging ocean colour observations seamlessly. *Ocean Challenge*, *21*(1).

Lévy, M., Ferrari, R., Franks, P. J. S., Martin, A. P., & Riviére, P. (2012). Bringing physics to life at submesoscale. *Geophysical Research Letters*, *39*(14), L14602. https://doi.org/10.1029/2012GL052756

Locarnini, R., Mishonov, A., Baranova, O., Boyer, T., Zweng, M., Garcia, H., et al. (2019). In *World Ocean Atlas 2018, volume 1: Temperature*. In *NOAA Atlas NESDIS* (Vol. 81, p. 52).

Mahadevan, A. (2014). Eddy effects on biogeochemistry. *Nature*, *506*(7487), 168–169. https://doi.org/10.1038/nature13048

Marchesiello, P., McWilliams, J. C., & Shchepetkin, A. (2003). Equilibrium structure and dynamics of the California current system. *Journal of Physical Oceanography*, *33*(4), 753–783. https://doi.org/10.1175/1520-0485(2003)33<753:esadot>2.0.co;2

McGillicuddy, J. D., Anderson, L. A., Bates, N. R., Bibby, T., Buesseler, K. O., Carlson, C. A., et al. (2007). Eddy/wind interaction stimulate extraordinary mid-ocean plankton blooms. *Science*, *316*(5827), 1021–1026. https://doi.org/10.1126/science.1136256

McGillicuddy, J. D., Robinson, A., Jannasch, H., Johnson, R., Dickey, T., McNeil, J., et al. (1998). Influence of mesoscale eddies on new production in the Sargasso Sea. *Nature*, *394*(6690), 263–266. https://doi.org/10.1038/28367

McWilliams, J. C., & Flierl, G. R. (1979). On evolution of isolated non-linear vortices. *Dynamics of Atmospheres and Oceans*, *5*, 43–66.

Meeuwis, J. M., & Lutjeharms, J. R. E. (1990). Surface thermal characteristics of the Angola-benguela front. *African Journal of Marine Science*, *9*(1), 261–279. https://doi.org/10.2989/025776190784378772

Nencioli, F., Dall'Olmo, G., & Quartly, G. (2018). Agulhas ring transport efficiency from combined satellite altimetry and Argo profiles. *Journal of Geophysical Research*, *123*(8), 5874–5888. https://doi.org/10.1029/2018JC013909

Ostrowski, M., da Silva, J. C. B., & Basik-Sangolay, B. (2009). The response of sound scatterers to El-Nino-La Nina-like oceanographic regimes in the southeastern Atlantic. *ICES Journal of Marine Science*, *63*, 1063–1072. https://doi.org/10.1093/icesjms/fsp102

Paulo, S., & Sato, O. T. (2015). Do eddies ride on Rossby waves? *Journal of Geophysical Research*, *120*(8), 5417–5435. https://doi.org/10.1002/2015JC010737

Penven, P., Échevin, V., Pasapera, J., Colas, F., & Tam, J. (2005). Average circulation, seasonal cycle and mesoscale dynamics of the Peru current system: A modeling approach. *Journal of Geophysical Research*, *110*(C10), C10021. https://doi.org/10.1029/2005JC002945

Peterson, R., & Stramma, L. (1991). Upper-level circulation in the South Atlantic Ocean. *Progress in Oceanography*, *26*, 1–73. https://doi.org/10.1016/0079-6611(91)90006-8

Pujol, M.-I., Faugere, Y., Taburet, G., Dupuy, S., Pelloquin, C., Ablain, M., & Picot, N. (2016). DUACS DT2014: The new multi-mission altimeter data set reprocessed over 20 years. *Ocean Science*, *12*(5), 1067–1090. https://doi.org/10.5194/os-12-1067-2016

Quartly, G. D., Buck, J. J. H., Srokosz, M. A., & Coward, A. C. (2006). Eddies around Madagascar - the Retroflection re-considered. *Journal of Marine Systems*, *63*(3–4), 115–129. https://doi.org/10.1016/j.jmarsys.2006.06.001

Raj, P. R., Chafik, L., Nilsen, J. E., Eldevik, T., & Halo, I. (2015). The Lofoten vortex of the Nordic Seas. *Deep-Sea Research, Part A: Oceanographic Research Papers I*, *96*, 1–14. https://doi.org/10.1016/j.dsr.2014.10.011

Raj, P. R., Johannessen, J. A., Eldevik, T., Nilsen, J. E., & Halo, I. (2016). Quantifying mesoscale eddies in the Lofoten Basin. *Journal of Geophysical Research*, *121*(7), 4503–4521. https://doi.org/10.1002/2016JC011637

Rhines, P. B. (1975). Waves and turbulence on a β plane. *Journal of Fluid Mechanics*, *69*(3), 417–443. https://doi.org/10.1017/s0022112075001504

Rio, M. H., Guinehut, S., & Larnicol, G. (2011). The new CNES-CLS09 global mean dynamic topography computed from the combination of GRACE data, altimetry and in-situ measurements [Dataset]. *Journal of Geophysical Research*, *116*, C07018. https://doi.org/10.1029/2010JC006505

Robinson, A. R. (1983). *Eddies in marine science* (p. 644). Springer-Verlag.

Rouault, M., Florenchie, P., Fauchereau, N., & Reason, C. J. (2003). South East tropical Atlantic warm events and southern African rainfall. *Geophysical Research Letters*, *30*(5), 8009. https://doi.org/10.1029/2002GL014840

Rouault, M., Illing, S., Bartholomae, C., Reason, C. J., & Bentamy, A. (2007). Propagation and origin of warm anomalies in the Angola Benguela upwelling system in 2001. *Journal of Marine Systems*, *68*(3–4), 473–488. https://doi.org/10.1016/j.jmarsys.2006.11.010

Schouten, M. W., Matano, R. P., & Strub, T. P. (2005). A description of the seasonal cycle of the equatorial Atlantic from altimeter data. *Deep-Sea Research, Part A: Oceanographic Research Papers I*, *52*(3), 477–493. https://doi.org/10.1016/j.dsr.2004.10.007

Souza, J. M. A. C., de Boyer Montegut, C., & Le Traon, P. Y. (2011). Comparison between three implementations of automatic identification algorithms for the qualification and characterization of mesoscale eddies in the South Atlantic Ocean. *Ocean Science*, *7*(3), 317–334. https://doi.org/10.5194/os-7-317-2011

Stammer, D., Wunsch, C., Giering, R., Eckert, C., Heimbach, P., Marotzke, J., & Marshall, J. (2002). Global ocean circulation during 1992-1997, estimated from ocean observations and a general circulation model. *Journal of Geophysical Research*, *107*(C9), 3118. https://doi.org/10.1029/2001JC000888

Stander, G. H. (1964). The Benguela Current off South West Africa. *irmrlswa*, *12*, 5–81.

Stegner, A., LeVu, B., Dumas, F., Ghannami, M. A., Nicolle, A., Durand, C., & Faugere, Y. (2021). Cyclone-anticyclone asymmetry of eddy detection on gridded altimetry product in the Mediterranean Sea. *Journal of Geophysical Research*, *126*(9), e2021JC017475. https://doi.org/10.1029/2021JC017475

Stramma, L., Bange, H. W., Czeschel, R., Lorenzo, A., & Frank, M. (2013). On the role of mesoscale eddies for the biological productivity and biogeochemistry in the eastern tropical Pacific Ocean off Peru. *Biogeosciences*, *10*(11), 7293–7306. https://doi.org/10.5194/bg-10-7293-2013

Stramma, L., & England, M. (1999). On the water masses and mean circulation of the South Atlantic Ocean. *Journal of Geophysical Research*, *104*, 20863–20883. https://doi.org/10.1029/1999jc900139

Theiss, J. (2004). Equatorward energy cascade, critical latitude, and the predominance of cyclonic vortices in geostrophic turbulence. *Journal of Physical Oceanography*, *34*(7), 1663–1678. https://doi.org/10.1175/1520-0485(2004)034<1663:eeccla>2.0.co;2

Tulloch, R., Marshall, J., & Smith, K. S. (2009). Interpretation of the propagation of surface altimetric observations in terms of planetary waves and geostrophic turbulence. *Journal of Geophysical Research*, *114*(C2), C02005. https://doi.org/10.1029/2008JC005055

Vallis, G. (2006). *Atmospheric and oceanic fluid dynamics* (p. 745). Cambridge University Press.

Willett, C. S., Leben, R. R., & Lavin, M. F. (2006). Eddies and tropical instability waves in the eastern tropical Pacific: A review. *Progress in Oceanography*, *69*(2–4), 218–238. https://doi.org/10.1016/j.pocean.2006.03.010

Wunsch, C. (2000). Toward a mid-latitude ocean frequency-wavenumber spectral density and trend determination. *Journal of Physical Oceanography*, *40*(10), 2264–2282. https://doi.org/10.1175/2010jpo4376.1

Zweng, M., Reagan, J., Seidov, D., Boyer, T., Locarnini, R., Garcia, H., et al. (2019). In *World Ocean Atlas 2018, volume 2: Salinity. A. Mishonov (Tech. Rep.)*. In *NOAA Atlas NESDIS* (Vol. 82, p. 50).

Erratum

In the originally published version of this article, the last sentence in the caption for Figure 4 was incomplete in the PDF. The sentence should read: "The intersection between R_D and L_R, identified by blue horizontal line in Figure 5b, defines the critical latitude occurring 11.4°S." This may be considered the authoritative version of record.